Enhanced photovoltaic effect derived from the regulation of Jahn–Teller distortion in a lattice compensation structure

Yaping Liu, Fei Guo, (iD) Bo Yang, and Shifeng Zhao[a] (iD)

AFFILIATIONS

School of Physical Science and Technology & Inner Mongolia Key Lab of Nanoscience and Nanotechnology, Inner Mongolia University, Hohhot 010021, China

[a]Author to whom correspondence should be addressed: zhsf@imu.edu.cn. Tel./Fax: +86 471 499 3141

ABSTRACT

Larger remanent polarization and lower optical bandgap play crucial roles in the ferroelectric photovoltaic effect. However, they are always mutually conditioning for almost perovskite material based orbital hybridization theories. Here, we design a lattice compensation structure, in which Eu was incorporated to strengthen J–T distortion of Mn–O octahedral in $BiFeO_3$–$BiMnO_3$ solid solution films due to relieved degeneracy; in turn, the distortion compensates the lattice shrink derived from Eu doping. A narrow bandgap of 2.24 eV and a large remanent polarization of 93.7 $\mu C/cm^2$ are achieved by lattice compensation modification. Compared with the film with an Eu doping concentration of 0.04, the open-circuit voltage and the short-circuit current of the film with 0.08 doping concentration are increased by 4.6 and 2.7 times, respectively, showing remarkable ferroelectric photovoltaic response. This work identifies an alternative strategy to enhance ferroelectric photovoltaic effects by regulating J–T distortion and lattice compensation.

Published under an exclusive license by AIP Publishing. https://doi.org/10.1063/5.0059359

Conventional semiconductor PN junction solar cells have attracted extensive attention due to their high photoelectric conversion efficiency.[1] However, the open-circuit voltage is restricted by the bandgap since the produced electron–hole pairs are separated by the internal field in PN junctions, which decreases further improvement in conversion efficiency.[2] Differently, photovoltaic voltage can exist in a homogeneous ferroelectric material under illumination by the depolarization field as the driving force to separate electron–hole pairs.[3] Therefore, the ferroelectric photovoltaic effect is a bulk effect with fascinating features such as an open circuit voltage free from the bandgap and a photocurrent proportional to the polarization magnitude.[4,5] Therefore, the remanent polarization and the optical bandgap play crucial roles in ferroelectric photovoltaic effects. The sufficient visible light can be absorbed by narrow bandgap materials to create electron–hole pairs that are separated by a high depolarization field.[6]

For most ABO_3 ferroelectric materials, the bandgap is much larger than that of semiconductors, which makes the absorption of light mainly concentrate in the ultraviolet region, while the absorption for visible light is at a low level. One of the reasons is that in most ferroelectric materials, the polarization and optical bandgap are mutually conditioning, in which strong orbital hybridization between the B-site

atoms and the oxygen atoms results in large polarization; however, this coupling effect with tight electron correlation generates a broad bandgap. Room-temperature multiferroic $BiFeO_3$ with a bandgap of 2.74 eV and large remanent polarization can alleviate the competition between the polarization and bandgap, because its ferroelectricity is mainly derived from the strong orbital hybridization of Bi6s-O2p, while the bandgap mostly is resulted from that of Fe3d-O5p.[7–9] However, the spectrum response of the photovoltaic effect still locates in the near ultraviolet region for such bandgaps. Therefore, several efforts had been made to reduce the optical bandgap, extending the visible light absorption.[10,11] However, the influence of ferroelectric polarization on the photovoltaic effect is ignored. Similar research is particularly focused on the efficient separation of electron–hole pairs by co-doping at A and B sites to increase polarization.[12] However, the bandgap was also broadened with the increase in polarization. Therefore, how to design a narrower bandgap and simultaneously obtain larger polarization is urgently needed.

Notably, Jahn–Teller (J–T) distortion is caused by the elimination of electron degeneracy in d orbitals of the central ion, which can regulate the bandgap. Meanwhile, the distortion intensifies the central asymmetry of positive and negative charges and improves the polarity.

The distortion offers an opportunity for narrowing the bandgap and enhancing polarization, and similar structural distortion regulation is also present in magnetic fields and other systems.[13–15] This Letter aims to introduce and regulate the J–T effect derived from Mn–O octahedral in $BiFeO_3$–$BiMnO_3$ solid solution films. The optimal proportion of $0.92BiFeO_3$-$0.08BiMnO_3$ is chosen on the basis of great ferroelectric property with stable leakage. Furthermore, in order to design a lattice compensation structure, the ion radius of the doping element should be smaller than that of Bi^{3+} (1.36 Å), so rare earth elements are candidates. Furthermore, Eu element is also selected to modify magnetic materials in other studies.[16] Therefore, Eu was incorporated with different proportions to strengthen the J–T distortion of Mn–O octahedral due to relieved degeneracy; in turn, the distortion compensates the lattice shrink derived from Eu doping. On the one hand, the enhanced J–T distortion induces the impurity energy level to move toward the conduction band, narrowing the bandgap. On the other hand, they both intensify the central asymmetry of positive and negative charges and compensate the lattice shrink derived from Eu doping, which is contributed to the larger polarization. Such regulations of the J–T distortion obtain a narrow bandgap of 2.24 eV and simultaneously a large remanent polarization of 93.7 $\mu C/cm^2$ in $0.92BiFeO_3$–$0.08BiMnO_3$-$0.08Eu$ solid solution films. The open-circuit voltage and the short-circuit current increase to 0.192 V and 14.3 $\mu A/cm^2$, respectively, demonstrating a considerable photovoltaic response. The mechanisms of the regulation of the J–T distortion on ferroelectric photovoltaic effects in this lattice compensation structure are discussed in detail.

The solid solution films were prepared by the sol-gel method. $Mn(CH_3COO)_3 \cdot xH_2O$, $Bi(NO_3)_3 \cdot 5H_2O$, $Fe(NO_3)_3 \cdot 9H_2O$, and $Eu(NO_3)_3 \cdot 6H_2O$ were dissolved into ethylene glycol methylether to form a solution. The doping proportions of Eu were set at 0.04, 0.06, 0.08, and 0.10. The precursor solutions were spun onto a Pt/Ti/SiO$_2$/Si (100) substrate to form the films. Crystals structures and valence states were characterized using x-ray diffraction (XRD, Brucker D8) and x-ray photoelectron spectroscopy (XPS). The ferroelectric properties are identified by the ferroelectric analyzer (Multi100V, RT). The Raman spectra were obtained by a Raman spectrometer (LABRAM H R800). The ultraviolet-visible reflection spectrum was analyzed by a Hitachi 3900 spectrophotometer, and a Keithley 2400 source meter was used to measure the current–voltage (J–V) characteristics and switching response under illumination conditions provided by a xenon lamp with the light intensity of ∼50 mW/cm^2 to simulate standard solar illumination.

Figure 1(a) presents XRD patterns of Eu doped BFO-BMO films. The diffraction peaks nicely match the standard card (ICSD-51662), showing rhombohedral *R3c* symmetry and no second impurity phases. All the diffraction peaks slightly move to high diffraction angles compared with the standard diffraction peaks of BFO (ICSD-186955) due to the less ionic radius of Mn^{3+} than that of Fe^{3+}. Interestingly, when Eu proportion is lower 0.1, the peak positions of Eu doped films are roughly consistent with those of BFO-BMO films, while they shift significant toward a higher angle when the doping proportion is 0.1, as shown in Fig. 1(b). Generally, the lattice would shrink when the smaller ionic radius of Eu^{3+} (1.226 Å) replaces the larger radius Bi^{3+} (1.36 Å) in the lattice. For further investigating the distortion characteristics, the tolerance factor is calculated according to the equation
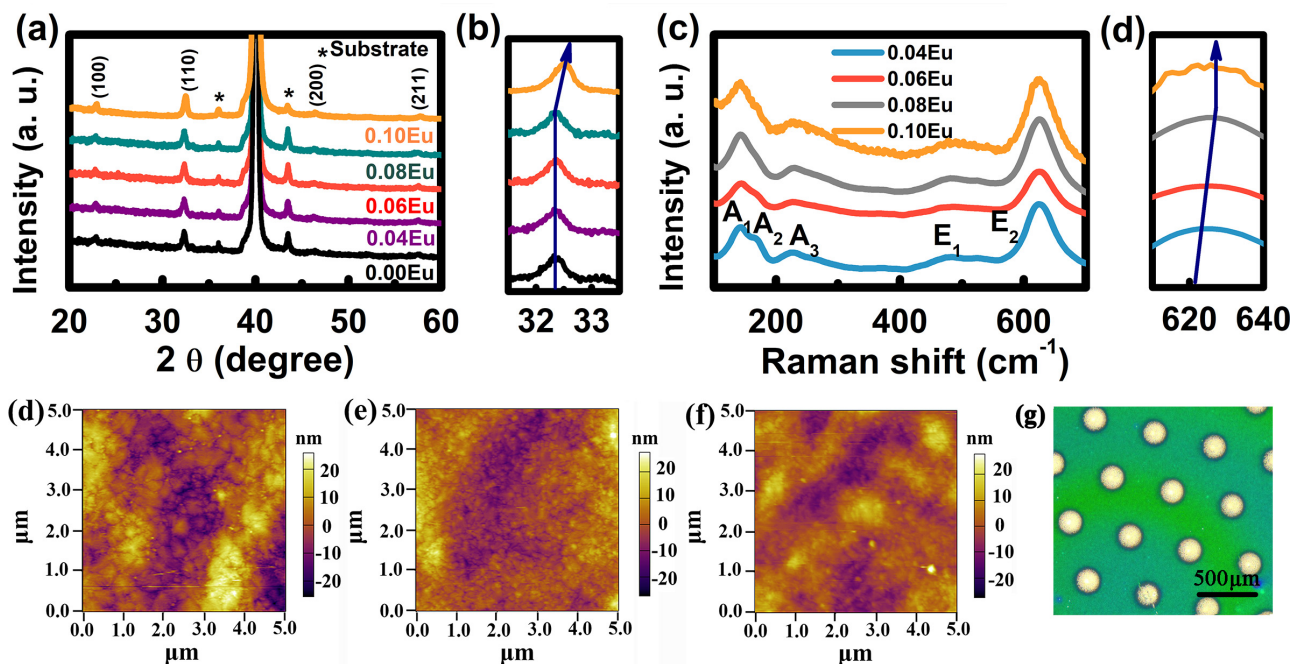

FIG. 1. (a) XRD patterns, (b) an enlarged view of the XRD pattern, (c) Raman shift of Eu doped BFO-BMO films, (d) enlarged Raman shift, AFM surface topography for (e) BFO-BMO-0.04Eu, (f) BFO-BMO-0.06Eu, (g) BFO-BMO-0.08Eu, and (h) top electrode image.

$$\tau = \frac{r(a) + r(o)}{\sqrt{2}(r(b) + r(o))}, \quad (1)$$

where $r(a)$, $r(b)$, and $r(o)$ are the average ionic radius of A-site ions (Eu^{3+} or Bi^{3+}), B-site ions (Fe^{3+} or Mn^{3+}), and oxygen ions, respectively. The tolerance factor values are 0.9543, 0.9525, 0.9516, 0.9506, and 0.9497 for the Eu proportions of 0.0, 0.04, 0.06, 0.08, and 0.10, respectively, in BFO-BMO solid solution films. The decrease means the lattice shrink. However, this phenomenon has not been observed in the films with Eu doping proportions lower than 0.1 due to the unchanged lattice parameters, which indicates a compensation behavior for the lattice shrink. The effect is caused by the J–T distortion of the Mn–O octahedron, where the octahedron disorder is enhanced to maintain the original unit cell.

The J–T effect of BFO-BMO-Eu films was confirmed by the Raman spectrum as shown in Fig. 1(c). The Raman active modes of A and E symmetries are summarized by the irreducible representation $\Gamma = 4A + 9E$.[17] The peaks at the positions of 140, 172, and 217 cm^{-1} correspond to A_1, A_2, and A_3 modes, respectively, and the remaining two peaks are designated as E modes. A_1, A_2, and A_3 modes are closely related to the vibrations of Bi-O bonds.[18] It is shown that the intensity of the A_2 peak decreases with the increase in the Eu concentration, which is in accord with the decline of the number of the Bi–O bond,[19] while E_1 and E_2 modes around 480 and 625 cm^{-1} are caused by the J–T distortion, which correspond to the antisymmetric and symmetrical stretching vibration mode of the Mn–O octahedron, respectively.[20] The appearance of E modes indicates the J–T distortion of the Mn–O octahedron due to the introduction of $BiMnO_3$. Especially, the magnified image of the Raman diffraction pattern near 625 cm^{-1} is shown in Fig. 1(d). It is worth noting that the E_2 peak first shifts slightly toward high frequencies from 624.54 to 624.94 cm^{-1} to 626.2 cm^{-1} and then maintains at 626.2 cm^{-1}, which is consistent with results reported in other studies,[21] indicating that the compressive stress on the Mn–O octahedron is gradually increasing to the limit and then remains unchanged, and the Mn–O bond length is gradually decreasing to remain constant with the increase in the Eu proportion. In other words, with appropriate doping, the J–T distortion of the Mn–O octahedron gradually increases, which is attributed to introduce degenerate energy levels. Compared with the Bi–O bond, weaker hybridization of the Eu–O bond generates new degenerate energy levels in the Mn–O

octahedral, which enhances the J–T distortion of the octahedral.[22] The J–T distortion compensates the lattice shrink derived from the smaller radius Eu substitution for Bi into the lattice, where the behavior is defined as a lattice compensation effect. That is to say, with the modest increase in Eu, the enhanced J–T distortion compensates the increasing lattice shrink, which maintains unchanged lattice parameters while excessive doping cannot form lattice compensation on account of defects and other factors. Therefore, we will focus the discussion on appropriately doped films. Aside from that the surface morphology and roughness of the films were collected through AFM as shown in Figs. 1(e)–1(g). It can be seen that all the films have smooth surfaces and uniform grain distribution. The average grain size gradually decreases, and the surface becomes denser with the increase in the Eu doping proportion. The radius of the gold electrode on the upper surface of the film sample is 0.1 mm as shown in Fig. 1(h).

Figure 2(a) displays XPS of Mn2p and the data fitting curves with different Eu doping proportions. Two peaks of the binding energy at 641.4 and 653 eV are in accord with 2p3/2 and 2p1/2 spin orbits of Mn^{3+}, respectively.[23] There is no split or other peaks, which demonstrates that Mn^{3+} does not change the valence state and remains stable in the crystal lattice after doping Eu. Figure 2(b) shows the XPS patterns of Fe2P. Two characteristic peaks, 710 and 724.2 eV, correspond to Fe2p3/2 and Fe2p1/2, respectively. A satellite peak peculiar to Fe appears between the two peaks. The Gauss–Lorentz function was used to fit the Fe2p3/2 peak. It is shown that the combined state of Fe is composed of Fe^{2+} and Fe^{3+}, and the corresponding peak positions are near 709.8 and 711.7 eV.[24] The relative proportions of Fe^{3+} and Fe^{2+} were revealed by an enclosed area above the yellow based line. Obviously, with the increase in the Eu proportion, the ratio of Fe^{3+}/Fe^{2+} gradually increases. According the reaction equation,

$$2Fe^{2+} \xrightarrow{Fe^{3+}} 2Fe^{2+'}_{Fe^{3+}} + V_O^{\cdot\cdot}, \quad (2)$$
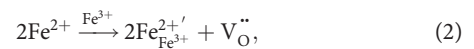
it indicates that the oxygen vacancy concentration gradually declines with the increase in Eu and the incorporation of Eu inhibits Fe^{3+} transfer to Fe^{2+}. Subsequently, the O1s spectrum was fitted to further clarify the content of oxygen vacancies. As shown in Fig. 2(c), the two binding states at 529 and 530.8 eV correspond to lattice oxygen (O_L) and oxygen vacancy (O_V), respectively.[25,26] As the doping proportion of Eu increases, the concentration of oxygen vacancies gradually
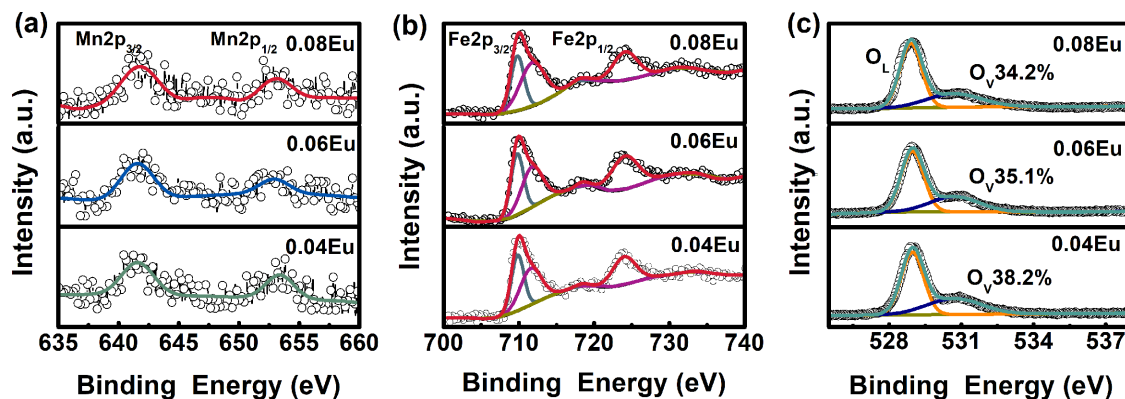

FIG. 2. XPS spectra of (a) Mn2p and the fitted spectra of (b) Fe2p and (c) O1s.

decreases from 38.2% for the films with 0.04 Eu doping to 34.2% for the films with 0.08 Eu doping. Trace to its cause, the addition of Eu eliminates the degenerate Mn–O octahedron and improves the stability of B-site ions, which reduces the oxygen vacancy in the film. Moreover, the decreasing grain size enhances the area of oxygen contacts, suppressing the formation of oxygen vacancies.

Figure 3(a) shows ferroelectric hysteresis loops of Eu doped BFO-BMO films. All films behave satisfactory remnant polarization, which is derived from the intensive shift of positive and negative charge centers in the rhombohedral phase. Interestingly, the maximum polarization (P_M) and remnant polarization (P_r) of the solid solution films first increase and then decrease at the same electric field with the increase in the Eu proportion. It is worth pointing out that the optimal P_r and P_M valves reach as large as 93.7 and 114.6 $\mu C/cm^2$ at Eu proportion of 0.08, which is very high compared with the other polycrystalline BFO-based thin film materials.[27,28] Furthermore, the BFO-BMO-0.10Eu film exhibits an imperfect "banana" ferroelectric hysteresis loop with P_r and P_M of 53.7 and 73 $\mu C/cm^2$, respectively, much lower than the other doping proportion. The specific changes of P_M and P_r with Eu doping proportions are shown in Fig. 3(b). The obviously enhanced polarization is ascribed to the decrease in the spatial symmetry due to the strengthened J–T distortion of the Mn–O octahedron in the lattice compensation structure, while the significant decrease in polarization is attributed to the defects and leakage in the film for excessive doping. Moreover, the lattice does not shrink after appropriately doping Eu, which compensates the rhombohedral structure with large dipole moment.

Figure 3(c) depicts the leakage current density (J) and electric field (E) curves of BFO-BMO-Eu solid solution films. Similarly, the leakage performances also show the trend of first improvement in the lattice compensation structures and then deterioration. In the lattice compensation structures, the leakage performances are gradually improved due to the reduction in defects and grain size. The

incorporation of Eu inhibits the valence state transformation of Fe^{3+} ions, reducing the generation of oxygen vacancies. The decrease in the grain size, accompanied by the gradual increase in the grain boundary, prevents electrons from moving, thus reduces the leakage. Nevertheless, when the excess doping proportion reaches 0.1, the leakage performance deteriorates sharply, closely relating to the defects in the film, as reflected in the leakage mechanism. lg(J)-lg(E) curves in Fig. 3(d) show that the slopes S are 1.43, 1.32, and 1.29 for the Eu proportions of 0.04, 0.06, and 0.08, respectively. It indicates that the main leakage mechanisms of BFO-BMO-Eu films in lattice compensation structures follow the Ohmic conduction mechanism ($S \sim 1$), accompanied by various sources of charge carriers when the slop tends to 2.[29] With increasing Eu proportions, the conduction mechanism of Ohm's law becomes more dominant, indicating that the density of free charge carriers injected into the films gradually decreases, which improves the insulation performances of the films. However, the slope S mutation is from 1.32 to 3.7 at 200 kV/cm² electric fields for BFO-BMO-0.10Eu films, which indicates that the main conduction mechanism transfers from the Ohm mechanism to Poole–Frenkel (PF) emission with the increase in the electric field. The transformation is caused by the large tilt of the conduction band at high fields, which makes the electrons on the impurity level be excited to the conduction band, and the number of charge carriers injected into the film increases sharply, resulting in the terrible leakage performance with an Eu doping concentration of 0.1.

The ultraviolet–visible reflection spectra in Fig. 3(e) show that the reflectance edges of the solid solution films are mainly concentrated in the visible light region, and with increasing Eu doping proportions, the reflectance of the films first decreases and then increases slightly. As a kind of the direct bandgap semiconductor, the bandgaps of BFO-BMO-Eu solid solution films calculated by the Kubelka–Munk equation are 2.29, 2.27, 2.24, and 2.26 eV for Eu proportions of 0.04, 0.06, 0.08, and 0.10, respectively, as shown in Fig. 3(f).[30]
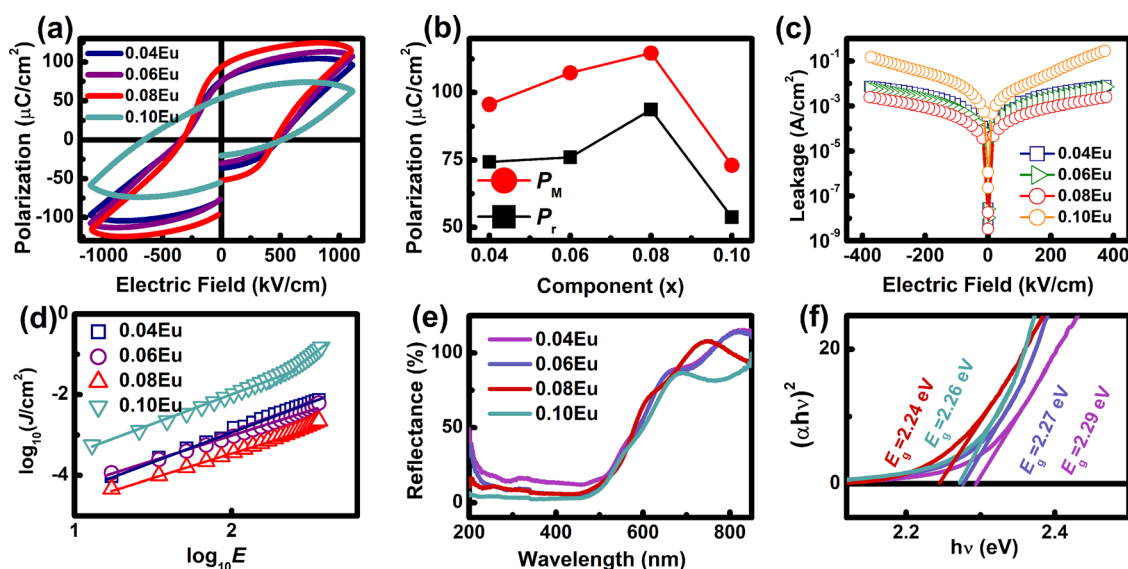

FIG. 3. (a) P–E loops of BFO-BMO-Eu solid solution films, (b) P_M and P_r with different doping proportions of Eu, (c) the leakage of BFO-BMO-Eu films, (d) log(J) vs log(E), (e) the ultraviolet–visible reflectance spectra of BFO-BMO-Eu films, and (f) the estimated bandgap.

The narrowing bandgap is attributed to the enhanced J–T distortion. First-principle calculation reveals that the bandgap of BFO mainly originates from Fe–O orbital hybridization.[31] The introduction of BMO in the lattice generates a new energy level structure, which narrows the bandgap of BFO. Further doping Eu, the weaker Eu–O bond breaks the coupling balance and generates degenerate energy levels in Mn–O octahedral, which induces intensive distortion in the Mn–O octahedron due to the J–T effect. The orbital hybridization configuration is rebuilt at the B-site, which reduces the gap between the impurity energy level and the conduction band, thus narrowing the bandgap. On the contrary, the abnormal increase in the bandgap in BFO-BMO-0.10Eu films is attributed to the fact that the electron-filled lower energy states in the conduction band preclude additional electronic transitions to the bottom of the conduction band with doping when the doping reaches a certain extent, which was caused by the Burstein–Moss effect derived from the Pauli exclusion principle.[32,33] Based on the above discussion, excessive doping is not suitable for the application of photovoltaic devices, which is not involved in the following discussion.

Figure 4(a) shows the spectral response of ferroelectric photovoltaic effects for the solid solution films. Obviously, the photoelectric effect under the light condition is observed, and the response peaks of photovoltaic effects are located in the visible light region. With the increase in the Eu proportion, the response peaks display a gradual red shift, which is attributed to the narrower bandgap reduced by the J–T effect. The increasing response for the visible light would promote much electron–hole pairs to be induced and enhance the photovoltaic effect. As shown in the strong dynamic current response at the polarization voltage of 40 V under the alternating state of light on or off in Fig. 4(b), where the dark current densities of three films are adjusted to the same baseline, the on–off effect demonstrates an obvious photoelectric response. Figure 4(c) displays the J–V curves of the solid

solution films at the polarization voltage of 40 V under dark and light conditions. The open circuit voltage is enhanced from 0.041 to 0.096 and 0.192 V, meanwhile the short circuit current from 5.21 to 8.13 and 14.3 μA/cm^2 with the increase in Eu proportions. The enhancement is ascribed to the decrease in the bandgap and the improvement of ferroelectric properties. To be specific, as the driving force of carrier separation, the depolarization field enables the electron–hole pair to be separated more effectively with the increasing polarization. The open-circuit voltage and the short-circuit current of the films vs the polarization voltage are shown in Figs. 4(d) and 4(e), respectively. It is shown that the open circuit voltage and the short circuit current of the same sample increase gradually with the polarization voltage, directly proving that the increase in polarization leads to the improvement in the electron hole pair separation ability. In addition, the decrease in the bandgap reduces the barrier height of photon absorption, so that more carriers are excited from the valence band to the conduction band. As shown in Fig. 4(f), with the gradual incorporation of Eu, the photocurrent intensity gradually increases, indicating the carrier density contributed to the photogenerated current. In other words, the narrowing of the bandgap will increase the photogenerated carrier concentration. Thus, the narrow bandgap and great depolarization can achieve excellent photovoltaic performance by increasing the carrier concentration and the separation efficiency of electron hole pairs. Moreover, such performances are comparable with other reported ferroelectric based solar cells by simply adjusting the film thickness, polarization electric field, top electrodes, or optical bandgap.[34–36]

Indeed, the lattice compensation effect plays an important role in the J–T distortion regulated photovoltaic effect, which is investigated by the Landau theory. It is suggested that the BFO material behaves the second-order ferroelectric phase transition. Thus, the free energy equation can be expressed by
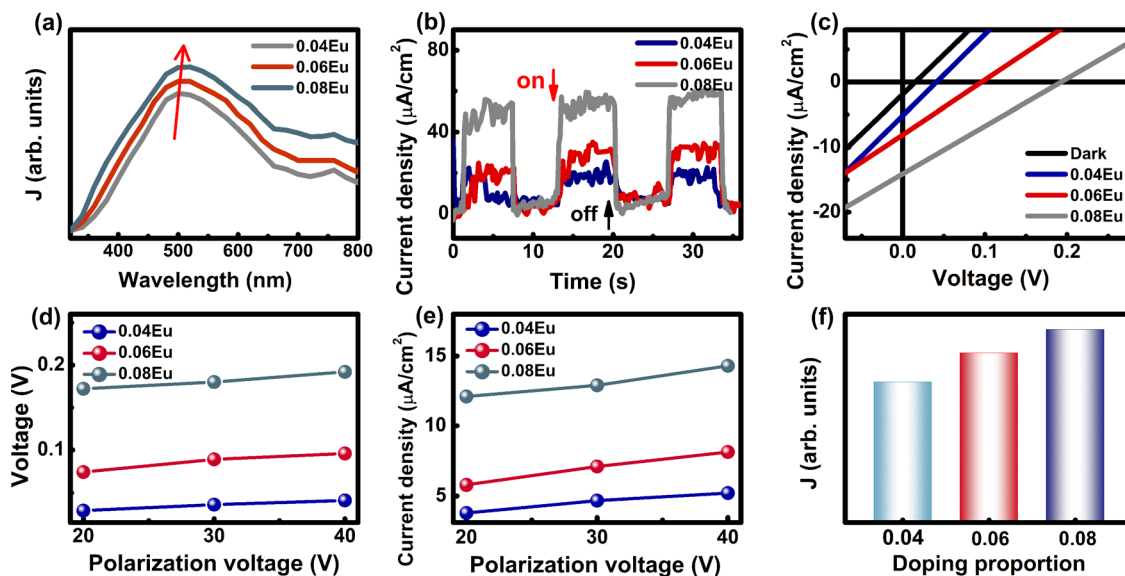

FIG. 4. (a) Spectral response of BFO-BMO-Eu solid solution films, (b) the switching response curves of the current density (J_{sc}) over time, (c) the dark and light J–V curves for BFO-BMO-Eu solid solution films, (d) the open circuit voltage, (e) the short circuit current with different polarization voltages, and (f) the Photocurrent intensity with different doping proportions.

$$W_{FE} = \frac{1}{2}\alpha_{FE}P^2 + \frac{1}{4}\beta_{FE}P^4 + \frac{1}{6}\gamma_{FE}P^6, \qquad (3)$$

where W_{FE} is the free energy, P is the polarization, and α, β, and γ are the Landau coefficients. According to the P–E curves in Fig. 3(a), W_{FE}-P curves of BFO and BFO-BMO-0.08Eu solid solution films are simulated in Fig. 5(a). The polarization at the bottom of W_{FE} represents the spontaneous polarization, expressed by

$$P_s = \sqrt{-\alpha_{FE}/\beta_{FE}}. \qquad (4)$$

BFO-BMO-0.08Eu solid solution films show the larger spontaneous polarization and lower extreme value of free energy. The lattice energy is regarded as the free energy to estimate the extreme value of free energy (W_{FE}). In order to evaluate it, the Castep model is applied to calculate the lattice energy in Materials Studio. Since the lattice parameter remains constant after doping Eu, $Bi_{0.83}Eu_{0.17}FeO_3$ supercell was used to approximate the incorporation of Eu on account of the convenience of calculation. The calculated lattice energies are -5.96×10^6 and -6.48×10^6 J/cm^3 in BFO and $Bi_{0.83}Eu_{0.17}FeO_3$ super cells, respectively. It indicates that $Bi_{0.83}Eu_{0.17}FeO_3$ has more stable structure and larger spontaneous polarization than the pure BFO. Therefore, the incorporation of element Eu is beneficial to improve polarization. Meanwhile, since the free energy represents the orbital hybridization stability between elements in the lattice, the lattice structure with lower energy presents intense electron interaction and needs larger excitation energy across the bandgap. Thus, Eu doped BFO may endure a broader bandgap like the most ferroelectric materials whose polarization and bandgap are mutually conditioning.

Oppositely, the actual bandgap based on the ultraviolet–visible reflection spectra decreases with the increase in Eu. The misjudgment of the computation is attributed to the fact that the evaluation derived from the Landau theory neglects the lattice compensation effect generated by the J–T distortion. The detailed modification process of the lattice compensation effect is displayed in Figs. 5(b)–5(d), where the BFO cubic crystal cell is adopted. As Eu is introduced in the BFO-BMO unit cell, the unit cell should shrink due to the smaller radius ion Eu^{3+} (1.226 Å) than Bi^{3+} (1.36 Å). However, the Mn–O octahedron generates larger J–T distortion due to the introduction of Eu, which

compensates the lattice shrink, as shown in Fig. 5(d). Noticeably, such a compensation structure not only intensifies the central asymmetry of positive and negative charges but also enhances the J–T distortion of the Mn–O octahedron and further induces the impurity energy level moving toward the conduction band. Thus, the polarization is strengthened, and the bandgap is narrowed.

In summary, the two mutually conditioning factors, both polarization and optical bandgap that decide ferroelectric photovoltaic performances, are optimized by regulating the J–T distortion in a lattice compensation structure. The J–T distortion of the Mn–O octahedron is enhanced by the incorporation of Eu into the A-site; simultaneously, this distortion compensates the lattice contraction, which not only causes the impurity level to move toward the Fermi level, resulting in the reduction of the bandgap, but also intensifies the central asymmetry of positive and negative charges by the lattice compensation effect, showing an increase in polarization. A narrow bandgap of 2.24 eV and a large remanent polarization of 93.7 μC/cm^2 are achieved in the 0.92BFO-0.08BMO-0.08Eu film. Correspondingly, it presents a considerable photovoltaic response with the open-circuit voltage and short-circuit current, increasing by 4.6 and 2.7 times with the film with an Eu doping concentration of 0.04, respectively. This work provides a feasible idea for improving the ferroelectric photovoltaic effect by regulating the John–Teller distortion in the lattice compensation structure.

AUTHOR DECLARATIONS

Conflict of Interest

The authors have no conflicts of interest to declare.

DATA AVAILABILITY

The data that support the findings of this study are available from the corresponding author upon reasonable request.

FIG. 5. (a) Relationship between the free energy (W_{FE}) and polarization (P) for BFO and BFO-BMO-0.08Eu and (b)–(d) the lattice compensation effect diagram.

REFERENCES

[1] K. Saron, M. Ibrahim, M. Hashim, T. Taha, N. Elfadill, E. Mkawi, and N. Allam, Appl. Phys. Lett. **118**, 023902 (2021).
[2] S. Svatek, C. Bueno-Blanco, D. Lin, J. Kerfoot, C. Macías, M. Zehender, I. Tobías, P. García-Linares, T. Taniguchi, K. Watanabe, P. Beton, and E. Antolín, Nano Energy **79**, 105427 (2021).
[3] Y. Bai, B. Yang, and S. Zhao, Appl. Phys. Lett. **115**, 261602 (2019).
[4] L. Jin, Y. He, D. Zhang, H. Zhang, M. Wei, and Z. Zhong, APL Mater. **7**, 121105 (2019).
[5] Y. Ji, T. Gao, Z. Wang, and Y. Yang, Nano Energy **64**, 103909 (2019).
[6] Y. Bai, J. Chen, X. Wu, and S. Zhao, J. Phys. Chem. C **120**, 24637 (2016).
[7] S. Clark and J. Robertson, Appl. Phys. Lett. **90**, 132903 (2007).
[8] F. Wang, S. Lv, C. Fu, and C. Zhang, Ferroelectrics **520**, 177 (2017).
[9] K. Liu, H. Fan, P. Ren, and C. Yang, J. Alloys Compd. **509**, 1901 (2011).
[10] P. Biswas, S. Pal, V. Subramanian, and P. Murugavel, Appl. Phys. Lett. **114**, 173901 (2019).
[11] Arti, S. Kumar, P. Kumar, R. Walia, and V. Verma, Results Phys. **14**, 102403 (2019).
[12] S. Gupta, M. Tomar, and V. Gupta, Mater. Des. **105**, 296 (2016).
[13] P. B. Marshall, K. Ahadi, H. Kim, and S. Stemmer, Phys. Rev. B **97**, 155160 (2018).
[14] K. Ahadi, X. Lu, S. Salmani-Rezaie, P. B. Marshall, J. Rondinelli, and S. Stemmer, Phys. Rev. B **99**, 041106 (2019).
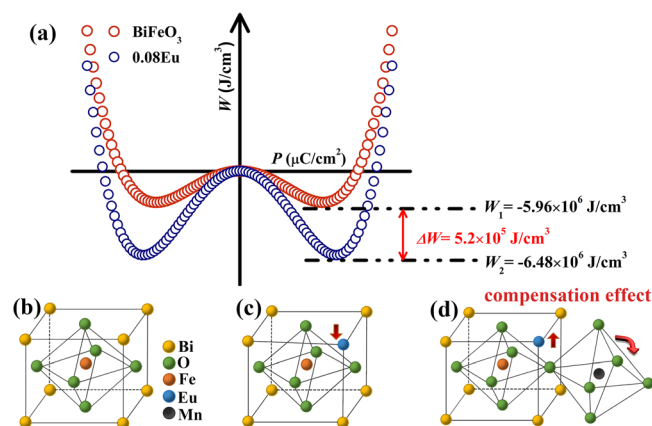[15] P. Marshall, H. Kim, and K. Ahadi, APL Mater. **5**, 096101 (2017).

[16]K. Ahadi, H. Kim, and S. Stemmer, APL Mater. **6**, 056102 (2018).

[17]M. Singh, H. Jang, S. Ryu, and M. Jo, Appl. Phys. Lett. **88**, 042907 (2006).

[18]G. Yuan, S. Or, H. Chan, and Z. Liu, J. Appl. Phys. **101**, 024106 (2007).

[19]F. Hardcastle and I. Wachs, J. Solid State Chem. **97**, 319 (1992).

[20]A. Lahmar, S. Habouti, M. Dietze, C. Solterbeck, and M. Essouni, Appl. Phys. Lett. **94**, 012903 (2009).

[21]G. Kartopu, A. Lahmar, S. Habouti, C.-L. Solterbeck, B. Elouadi, and M. Es-Souni, Appl. Phys. Lett. **92**, 151910 (2008).

[22]F. Chiang, M. Chu, F. Chou, H. Jeng, H. Sheu, F. Chen, and C. Chen, Phys. Rev. B **83**, 245105 (2011).

[23]S. Thakur, K. Singh, and O. Pandey, Mater. Chem. Phys. **187**, 96 (2017).

[24]T. Schedel-Niedrig, W. Weiss, and R. Schlogl, Phys. Rev. B **52**, 17449 (1995).

[25]Y. Rim, D. Kim, W. Jeong, and H. Kim, Appl. Phys. Lett. **97**, 233502 (2010).

[26]B. Luo, J. Appl. Phys. **122**, 195104 (2017).

[27]C. Chen, J. Her, and T. Pan, J. Phys. Chem. Solids **152**, 109986 (2021).

[28]T. Cao, J. Dai, and X. Wang, Ceram. Int. **46**, 7954 (2020).

[29]C. Wang, M. Takahashi, H. Fujino, X. Zhao, E. Kume, T. Horiuchi, and S. Sakai, J. Appl. Phys. **99**, 054104 (2006).

[30]Y. Sun, F. Guo, J. Chen, and S. Zhao, Appl. Phys. Lett. **111**, 253901 (2017).

[31]N. Gao, C. Quan, Y. Ma, Y. Han, Z. Wu, W. Mao, J. Zhang, J. Yang, X. Li, and W. Huang, Physica B **481**, 45 (2016).

[32]W. Zhou, H. Deng, H. Cao, J. He, J. Liu, P. Yang, and J. Chu, Mater. Lett. **144**, 93 (2015).

[33]X. Liang and J. Dai, J. Alloys Compd. **886**, 161168 (2021).

[34]G. Chen, K. Zou, Y. Yu, Y. Zhang, Q. Zhang, Y. Lu, and Y. He, Ceram. Int. **46**, 4148 (2020).

[35]B. Chen, M. Li, Y. Liu, Z. Zuo, F. Zhuge, Q. Zhan, and R. Li, Nanotechnology **22**, 195201 (2011).

[36]C. Elicker, L. Gularte, M. Moreira, S. Cava, and A. Feteira, Mater. Lett. **221**, 326 (2018).